261 (2026) 214429

Contents lists available at ScienceDirect

Geoenergy Science and Engineering

journal homepage: www.sciencedirect.com/journal/geoenergy-science-and-engineering

Modeling CO_2 flow through faulted/fractured reservoirs using tEDFM in corner-point grids

H.U. Rashid [a], C.S. Igweonu [b], O.M. Olorode [b,*], A.A. Abdullah [b], F. Olalotiti [c]

[a] Earth and Environmental Sciences Division, Los Alamos National Laboratory, Los Alamos, NM, 87545, USA
[b] Louisiana State University, Baton Rouge, LA, 70803, USA
[c] Intel Corporation, Santa Clara, CA, USA

HIGHLIGHTS

- Proposed transient EDFM for fractured corner-point grids.
- Demonstrated that using fault multipliers accounts only for flow across fault surfaces.
- The proposed model enables the modeling of flow both along and across fault surfaces.
- Results show that natural fractures or damage zones near faults can increase CO_2 leakage through caprocks.
- Mixed reality visualization facilitates the observation of the CO_2 migration path.

ARTICLE INFO

Keywords:
Underground CO_2 storage
CO_2 leakage
Flow along faults/fractures
tEDFM in corner-point grids
Mixed reality

ABSTRACT

The interest in underground CO_2 storage has increased significantly over the last decade because of the rising concern about global warming due to the growing levels of greenhouse gases in the atmosphere. Considering that CO_2 accounts for 80% of these greenhouse gases, carbon capture, utilization, and storage (CCUS) is regarded as one of the most direct approaches to achieving the net zero carbon target. Although CO_2 storage in deep saline aquifers and depleted gas reservoirs has been studied extensively, most studies use commercial simulators that model faults/fractures by simply modifying the transmissibility in the direction perpendicular to the fault surfaces. This work shows that this simplistic approach ignores the accelerated flow in the directions parallel to the fault plane, leading to significantly higher leakage along the fault surface. To accurately model the flow of CO_2 in faulted reservoirs, we present the first transient embedded discrete fracture model for corner-point grids (tEDFM-CPG). By comparing the results of the tEDFM-CPG to high-resolution reference solutions, we show that this approach is accurate and efficient at predicting CO_2 flow in faulted/fractured reservoirs. Finally, this work presents the use of mixed reality (MR) to efficiently observe CO_2 gas migration in the interior of these corner-point grid systems.

1. Introduction

Geologic CO_2 storage (GCS) has recently gained much attention because it is vital for curtailing climate change and global warming. Krevor et al. (2023) projects an exponential increase in CO_2 injection over the next few decades as part of the ongoing efforts to achieve the Intergovernmental Panel on Climate Change (IPCC) goals. Subsurface geological formations present numerous opportunities for safe and long-term CO_2 storage (Eiken et al., 2011). Potential storage sites include depleted hydrocarbon reservoirs (Li et al., 2006; Zhang et al., 2025), saline aquifers (Bentham and Kirby, 2005; Michael et al., 2009), and unmined coal seams (Shi and Durucan, 2005; Jiang et al., 2022). Of these alternatives, saline aquifers offer the largest storage capacities (Bachu, 2002). CO_2 injected into these formations can be trapped via various mechanisms, such as structural or stratigraphic trapping, residual trapping, dissolution trapping, and mineral trapping (Benson and Cole, 2008).

Structural trapping occurs when the injected CO_2 rises via buoyancy to the top of the permeable formation it is injected into and gets trapped by the cap rock. In contrast, residual trapping occurs when

* Corresponding author.
Email address: folorode@lsu.edu (O.M. Olorode).

https://doi.org/10.1016/j.geoen.2026.214429
Received 7 June 2025; Received in revised form 16 November 2025; Accepted 17 February 2026
Available online 20 February 2026
2949-8910/

Nomenclature

$A_{if\perp x}$	= area of fracture projections along each dimension, L^2, m^2
A_{ij}^{p}	= projection area, L^2, m^2
A^{nnc}	= area of a non-neighboring connection, L^2, m^2
d^{nnc}	= non-neighboring connection distance, L, m
k_f	= fracture permeability, L^2, m^2
k_m	= matrix permeability, L^2, m^2
k^{nnc}	= permeability of a non-neighboring connection, L^2, m^2
K_i	= vapor-liquid equilibrium constant for component i
R	= residual, $M^{-1}L^{-3}$, $kg^{-1}m^{-3}$
S^α	= saturation of phase, α
T_i	= half transmissibility, L^3, m^3
T^{nnc}	= transmissibility factor for a NNC, L^3, m^3
q^α	= volumetric flow rate of phase α, L^3/T, m^3/s
$\vec{x}_e$	= the grid block sizes in the X, Y, and Z directions, L, m
$\vec{x}$	= X, Y, and Z coordinates, L, m
x_i	= mole-fraction of component i in the liquid phase
X_i^α	= mass-fraction of component i in phase α
Y_i	= mass-fraction of component i in the gas phase
y_i	= mole-fraction of component i in the gas phase
Z_i	= overall mass-fraction of component i
ϕ	= porosity
ρ	= density, M/L^3, kg/m^3
t	= time, T, s

Subscripts

f	= fracture
m	= matrix
$M-M$	= interaction between two different host matrix cells
$pM-F$	= interaction between a projection matrix and a fracture cell
i, j	= cell indices
if	= interaction between matrix cell i and fracture cell f
α	= fluid phase

Superscripts

$k+1$	= current time step
nnc	= non-neighboring connections

the CO_2 plume migrates and rises, but the saturation of the formation through which it flows does not reduce below the residual gas saturation (Ide et al., 2007). Dissolution trapping begins when supercritical CO_2 comes into contact with the undersaturated brine in the reservoir, causing densification of the brine and initiating density-driven convection after injection (Emami-Meybodi et al., 2015; Neufeld et al., 2010). Additionally, dissolved CO_2 reacts with water to form carbonic acid, which triggers mineral dissolution or precipitation in the rock (Dai et al., 2020). As saline aquifers typically comprise sandstone formations dominated by quartz, geochemical reactions contributing to mineral trapping are minimal (Gunter et al., 2000).

It is worth noting that the different trapping mechanisms operate over different time scales, and some are more effective at permanently storing the injected CO_2 than others. For instance, structural trapping tends to be the dominant storage mechanism over relatively shorter time frames, but it is the most vulnerable to CO_2 leakage through faults/fractures running through the storage and cap rocks. The next fastest trapping mechanism is the residual or hysteresis trapping, which is also prone to CO_2 leakage if the residual gas saturation changes. As expected, the dissolution trapping mechanism is slower than the residual trapping but less prone to leakage. Finally, the mineral trapping mechanism is the safest way to sequester CO_2 in geologic formations permanently, but it is typically very slow– lasting hundreds to thousands of years.

One of the critical goals in GCS projects is to ensure that the injected CO_2 does not leak into shallower freshwater aquifers, which typically serve as drinking water sources. It is essential to model the CO_2 transport accurately to achieve this goal. Unfortunately, some authors have shown that the state-of-the-art subsurface numerical modeling techniques are inadequate at predicting observed CO_2 plume migration in the subsurface (Cavanagh and Haszeldine, 2014; Ringrose et al., 2009). There is a consensus that CO_2 plume migration is typically more heterogeneous than most simulation models indicate. To address this limitation, Ringrose et al. (2009) indicated that this could be because of faults/fracture networks, among other uncertainties in reservoir characterization. A peculiarity in the physics of CO_2 plume migration is the combination of buoyancy and CO_2/water mobility contrast (Bryant et al., 2008). In such systems, the preferential flow of CO_2 along (or in the direction parallel to the surface of) fault crevices controls the CO_2 plume migration. Unfortunately, the state-of-the-art reservoir simulators only model the flow across such faults using fault-transmissibility multipliers (Manzocchi et al., 2008; Pettersen, 2006). The omission of the flow along the faults leads to an underestimation of the transport of CO_2 in these simulation models because the buoyant CO_2 preferentially migrates along these conductive pathways. Therefore, similar to the failure of conventional simulators to predict water production in faulted reservoirs connected to aquifers (Fisher and Jolley, 2007), failure to account for accelerated along-fault CO_2 flow can result in substantially lower leakage rates relative to the actual leakage.

Commercial reservoir simulators typically use corner-point grids to accurately represent actual field reservoir geometries. These grids are constructed using a series of coordinates and depths that facilitate the creation of reservoir or structural models (Wadsley, 1980). Each grid block's eight vertices are individually specified in a corner-point grid, offering a more flexible definition of cell geometries than Cartesian grids. This flexibility enables the representation of various geological features, such as sloping faults/fractures, cross-stratified beds, and complex reservoir boundaries (Ding and Lemonnier, 1995). Of these geological features, faults and fractures are ubiquitous and are present in virtually all geologic rocks to some extent. Although it is possible to adjust coordinate lines to represent the orientations of a limited number of fractures in corner-point grids, explicitly gridding all fractures in such a manner is challenging and unrealistic. Therefore, an efficient approach is needed to simulate fractures effectively in corner-point grids.

The Embedded Discrete Fracture Model (EDFM) was developed to accurately and efficiently model fractures in standard reservoir simulators. It involves meshing the matrix and fractures independently and uses non-neighboring connections (NNCs) to account for the connectivity between the matrix and fracture cells. This approach does not require the matrix mesh to conform to the geometry of the fractures in the domain. EDFM was initially proposed for modeling conductive faults (Lee et al., 2000, 2001), but it has been extended by several researchers (Li et al., 2008; Hajibeygi et al., 2011; Moinfar et al., 2013; Olorode et al., 2020; Rashid et al., 2022; Rashid and Olorode, 2024). An advantage of EDFM is its compatibility with traditional reservoir simulators, making it widely applicable. However, applying EDFM to corner-point grids presents challenges due to the grids' irregular geometries and specialized block connections that complicate the transmissibility calculation. Xu and Sepehrnoori (2019) proposed an algorithm for EDFM in general corner-point grids with complex geometries (EDFM-CPG).

Although EDFM has found applications in modeling naturally fractured reservoirs, its assumption of linear pressure dependence in the matrix/fracture transfer term may introduce significant errors, especially when the matrix permeability is extremely low. Rao et al. (2019a) proposed using local grid refinements and boundary integral (Rao et al., 2019b) equations to address this issue. However, these methods are computationally expensive. Therefore, Olorode and Rashid (2022) introduced an analytical modification, which multiplies the standard NNC matrix/fracture flux term by a transient factor, as in dual continuum models. This transient NNC term is applicable at both early and late times. Their modified EDFM model, called the transient EDFM (tEDFM) method, was implemented for Cartesian grids.

This work addresses the knowledge gaps discussed in this section by presenting a tEDFM method developed for corner-point grids (tEDFM-CPG). Relative to the state of the art standard EDFM and its corner-point implementation (EDFM-CPG), the proposed tEDFM-CPG introduces a transient factor T_f that multiplies the matrix–fracture non-neighboring connection (NNC) flux, replacing the pseudo-steady transfer assumption with a formulation that is valid at both early and late times. This correction yields an improvement in prediction without local refinements, which means that tEDFM-CPG delivers the accuracy of refined/explicit models at the cost of an unrefined model, an essential capability when assessing the feasibility of a field-scale storage site with faults and fractures. tEDFM-CPG provides a flexible and efficient model for accurately predicting CO_2 transport along and across faults and fractures in caprocks and storage rocks at the field scale. To show the significance of the proposed model, we compared the results of CO_2 transport with and without accounting for the flow along fault surfaces using the Johansen formation, which is a faulted reservoir. The remaining sections of this paper discuss the governing equations for tEDFM-CPG, its verification against high-resolution reference solutions, its application to CO_2 leakage through fractured caprocks and storage rocks, and the study of CO_2 leakage along and across the large faults within the Johansen formation.

2. Governing equations

This section discusses our implementation of the transient Embedded Discrete Fracture Model (tEDFM) for corner-point grids using the MATLAB Reservoir Simulation Toolbox (MRST) (Lie, 2019). Xu and Sepehrnoori (2019) demonstrated the use of EDFM in corner-point grids. In this work, we implemented the tEDFM model in corner-point grids by extending the standard hierarchical fracture model (HFM) module in MRST to work with corner-point grids. Next, we incorporated the analytical EDFM modification presented in Olorode and Rashid (2022) into the EDFM model for corner-point grids. CO_2 injection, migration, and structural trapping mechanisms are modeled using a two-phase, two-component, water-gas model, where the “gas” phase corresponds to supercritical CO_2. This approximation is widely adopted in reservoir simulation (Pruess et al., 2005) because supercritical CO_2 behaves as a compressible fluid under storage conditions (Metz et al., 2005). The values of the density and viscosity in each grid block were obtained by interpolating tabulated values from Span and Wagner (1996) and Laesecke and Muzny (2017), respectively. These references account for the supercritical behavior of CO_2 and are implemented in CoolProp (Bell et al., 2014).

The mass conservation equation for phase (α), which refers to either the gas (g) or water (w) phase is given as:

$$\frac{\partial}{\partial t}(\phi\rho_\alpha S_\alpha) + \nabla\cdot(\rho_\alpha\vec{v}_\alpha) - \rho_\alpha q_\alpha/V = 0, \tag{1}$$

where ϕ, ρ_α, S_α, q_α, and V represent the porosity, mass density of phase α, phase saturation, phase rate, and grid block bulk volume, respectively. The Darcy velocity for any phase α ($\vec{v}_\alpha$) is given as follows:

$$\vec{v}_\alpha = -\mathbf{K}\frac{kr_\alpha(S_\alpha)}{\mu_\alpha}(\nabla p_\alpha - \rho_\alpha\mathbf{g}\nabla z) = -\mathbf{K}\lambda_\alpha(\nabla p_\alpha - \rho_\alpha g\nabla z). \tag{2}$$

Here, $\mathbf{K}$, kr_α, μ_α, p_α, $\mathbf{g}$, z, and λ_α represent the absolute permeability, relative permeability of phase α, phase viscosity, phase pressure, acceleration due to gravity, depth, and phase mobility. The phase mobility is defined as the ratio of the relative permeability of phase α to its phase viscosity, μ_α. Additionally, the constraints that the water and gas saturations sum up to one and the definition of the water-gas capillary pressure complement these governing equations. This yields two equations in two unknowns: gas-phase pressure and water saturation. Like the standard EDFM, tEDFM uses non-neighboring connections (NNCs) to handle fluid exchange between a fracture cell and its host matrix cell. It is implemented by adding a non-neighboring connection flux q_{nnc} to the governing equations in Eq. (1), as follows:

$$\frac{\partial}{\partial t}(\phi\rho_\alpha S_\alpha) + \nabla\cdot(\rho_\alpha\vec{v}_\alpha) - \rho_\alpha q_\alpha/V + q_{nnc}/V = 0, \tag{3}$$

where q_{nnc} represents the non-neighboring connection flux. Olorode and Rashid (2022) provide further details on the mathematical model and implementation of the tEDFM in Cartesian grids, but this work extends it for application in corner-point grids. We use the idea presented by Zimmerman et al. (1993) to model transient flow between matrix and fracture continua in dual-continuum models. They showed that the standard shape factor (σ_P) in the dual-continuum model is based on a pseudo-steady state assumption and is only valid at late times. They used the Vermeulen (1953) approach to obtain a transient factor (T_f), which can be multiplied with the pseudo-steady state shape factor to obtain the transient shape factor (σ_T), as in (Azom and Javadpour, 2012; Olorode, 2017):

$$\sigma_T = \sigma_P\, T_f, \tag{4}$$

where the transient factor can be written as:

$$T_f = \frac{2\Phi_i - \left(\Phi_m + \Phi_f\right)}{2\left(\Phi_i - \Phi_m\right)}. \tag{5}$$

In this equation, Φ_i represents the flow potential at initial conditions, whereas Φ_m and Φ_f represent the flow potentials in the host matrix and fracture cells, respectively. Based on Zimmerman et al. (1993), Azom and Javadpour (2012) showed that multiplying the pseudo-steady state transient factor by the transient factor yields a transient factor that is applicable at both early and late times. Considering the striking similarity between the pseudo-steady state matrix/fracture coupling term and the matrix/fracture NNC flux in EDFM, we multiplied the NNC flux by the transient factor. Therefore, the transient non-neighboring connection flux is given as follows:

$$q^{nnc} = T_f\sum_{m=1}^{N_{nnc}} A_m^{nnc}\frac{\rho k_m^{nnc}}{\mu}\left(\frac{\Phi - \Phi_m^{nnc}}{d_m^{nnc}}\right), \tag{6}$$

where T_f is as given in Eq. (5), and k^{nnc}, A^{nnc}, and d^{nnc} represent the permeability, area, and distance of the non-neighboring connections (NNCs), respectively. The symbol N_{nnc} is the number of NNCs for each cell, and p_j^{nnc} is the pressure of its non-neighboring cell. The transmissibility factor between each pair of cells in an NNC is given as:

$$T^{nnc} = \frac{k^{nnc}A^{nnc}}{d^{nnc}}. \tag{7}$$

There are four possible transmissibilities or connections between all types of cells in a fractured reservoir. These are the matrix-fracture, intersecting fracture, fracture-fracture, and matrix-matrix connectivities. However, only the first two are technically non-neighboring connections because the fracture-fracture and matrix-matrix connectivities are standard transmissibilities between two neighboring fracture cells and two neighboring matrix cells, respectively.

For matrix-fracture NNCs, the equations for A^{nnc}, k^{nnc}, and d^{nnc} are the same as those for EDFM in structured grids, as in Moinfar (2013):

$$A^{nnc} = 2A_f, \tag{8}$$

$$k^{nnc} = \frac{k_m\ k_f}{k_m + k_f}, \tag{9}$$

$$d^{nnc} = \frac{\int_v x_n dv}{V}. \tag{10}$$

It is worth noting that although the equation for A^{nnc} is the same as for EDFM in structured grids, the procedure to compute A_f in Eq. (8) is fundamentally different in the case of corner-point grids. Specifically, we need a more robust approach to compute A_f, which is the area of the intersection between the polygonal fracture and the polyhedral matrix cell. To this end, we implemented the algorithm presented in Appendix A of Xu and Sepehrnoori (2019) in MRST.

For intersecting fracture NNC, the transmissibilities are calculated exactly as for EDFM in structured grids, as follows Moinfar (2013):

$$T^{nnc} = \frac{T_1\ T_2}{T_1 + T_2}, \tag{11}$$

where T_1 and T_2 are half transmissibilities given as:

$$T_1 = \frac{k_{f1}\omega_1 L_{int}}{d_{f1}}, \tag{12}$$

and

$$T_2 = \frac{k_{f2}\omega_{f2} L_{int}}{d_{f2}}. \tag{13}$$

In these equations, L_{int} is the length of the intersection line between two fracture cells that intersect in a matrix cell. The symbols k_f and ω_f represent the fracture permeability and fracture aperture, whereas d_{f1} and d_{f2} represent the distances from the intersection line to the centroids of fracture cells 1 and 2.

As in Olorode and Rashid (2022), we solved the governing equations presented in this section by discretizing them in time and space using the backward finite difference and finite volume difference schemes, respectively. The discretized system of equations is then linearized and solved simultaneously using Newton's method and a linear solver such as the Generalized Minimum Residual solver. Discretizing and solving these governing equations is facilitated using MRST (Lie, 2019).

Although MRST was developed to work with corner-point grids, among other grid types, its "hfm" and "shale" modules are limited to Cartesian grids. Therefore, the tEDFM model presented in Olorode and Rashid (2022) cannot be applied to corner-point grids, which are state-of-the-art in simulating subsurface reservoirs. We first extended the "hfm" module to work with corner-point grids using the algorithm presented in Xu et al. (2019) to address this limitation. The modification of the "hfm" module enabled the use of EDFM with corner-point grids. In this work, we incorporated the analytical modification of EDFM for transient flow into the MRST "CO_2-lab" module to facilitate the efficient and accurate modeling of CO_2 flow along and across faults and fractures at early and late times and in corner-point grids. The next section discusses our verification of the modified codes against reference solutions obtained from high-resolution, fully dimensional fracture models.

3. Model verification

Although this section focuses on verifying the tEDFM-CPG model for CO_2 flow in geologic rocks, we start by illustrating the limitations of EDFM in unrefined corner-point grids. To this end, we simulated water production from a single-phase water reservoir with a vertical fault near the middle of a simple domain meshed with corner-point gridding. Table 1 summarizes the model parameters used. The four different approaches employed in simulating this problem include using–(a) a fully dimensional or explicit model, which uses a high-resolution mesh (shown in Fig. 1(b)) to model the fractures explicitly as 3D cells with a thickness equal to the fracture aperture, (b) EDFM in the unrefined corner-point grid in Fig. 1(a) and (c) EDFM in the refined corner-point grid in Fig. 1(b) and (d) tEDFM in the unrefined corner-point grid in Fig. 1.

Table 1
Reservoir model parameters for tEDFM verification.

Reservoir parameters	Value	Unit
Reservoir dimension	[1000 600 100]	m
Initial reservoir pressure, P_i	5700	psi
Flowing bottomhole pressure, P_{wf}	1000 psi	psi
Fracture half-length, x_f	656.16	ft
Fracture height, h_f	262.47	ft
Fracture width, w_f	0.01	ft
Fracture permeability, k_f	50	D
Fracture porosity, ϕ_f	0.5	–
Matrix permeability, k_m	2	μD
Matrix porosity, ϕ_m	0.16	–
Well radius, r_w	0.32	ft

The simulated water production rates using the four different approaches are summarized in Fig. 2(a). In contrast, Fig. 2(b) presents the percentage error of the three EDFM-based approaches relative to a high-resolution explicit model, which is the reference solution. The "EDFM" case in Fig. 2 refers to the use of EDFM in the unrefined corner-point grid. It shows a significant error (up to 87%) at early times because of the pseudo-steady state assumption implicit in the standard EDFM NNC flux. At this 87% error, the reference solution is 3614 bbl/day, whereas that of the EDFM model is 483 bbl/day. This indicates that the EDFM model is off by approximately one order of magnitude. In contrast, using EDFM in the refined corner-point grid (EDFM-Refined) yields production rates that match the reference solution but at approximately the same computational cost as the reference explicit model. This is because the EDFM-Refined model uses the same mesh as the explicit model, except that it treats the fracture as a 2D plane rather than a 3D slab, as in the explicit model. The tEDFM model shows a good match relative to the reference solution, even though it uses the same unrefined corner-point grid used in the EDFM model. This confirms the accuracy of the proposed analytical modification in unrefined corner-point grids.

Most commercial petroleum reservoir simulation packages multiply the transmissibility across faults as a technique to model faulted reservoirs. Appendix A presents a case involving water displacing oil in a simple reservoir with only one fault to demonstrate the errors introduced by using this approach. The reservoir is modeled using the transmissibility multiplier approach and the proposed tEDFM approach in corner-point grids. Table A.1 of the Appendix presents the reservoir model parameters used, whereas Figs. A.1–A.3 present the simulation grid, water saturation profile at the end of the simulation, and the water production rate, respectively.

The rest of this model verification section focuses on validating a field case involving CO_2 injection in the Johansen reservoir. No faults or fractures are considered here because the goal is to validate the base case (without faults/fractures) against a commercial compositional simulator with a robust CO_2 module. Fig. 3(a) presents the corner-point grid for the Johansen field, which is offshore of the southwestern coast of Norway. The model parameters are summarized in Table 2.

The porosity, horizontal and vertical permeability of all 11 layers of the Johansen field are presented in Figs. 3(b)–(d). These images show that the bottom six layers are the permeable sand layers, whereas the top five layers are the sealing caprocks. To quantify the CO_2 leakage through the faults into shallower formations, we artificially increased the horizontal permeability of the topmost layer. Therefore, it essentially represents shallower sands above the target reservoir sand for CO_2

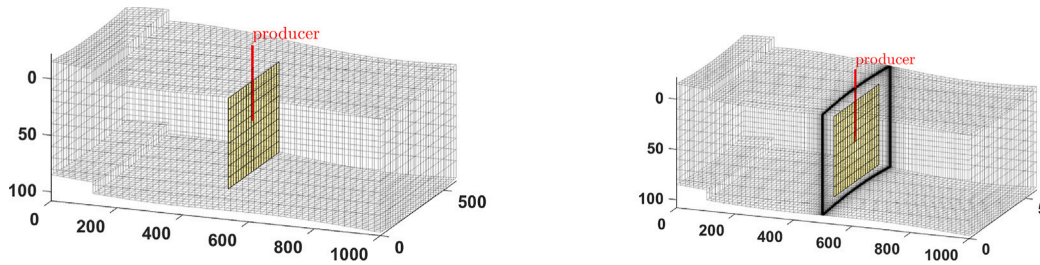

(a) Unrefined corner-point grid

(b) Refined corner-point grid

Fig. 1. The left image shows an unrefined corner-point grid with a fracture in the middle of the domain, whereas the right image shows a modified version of the corner-point grid with geometrically spaced grids near the fracture surface.

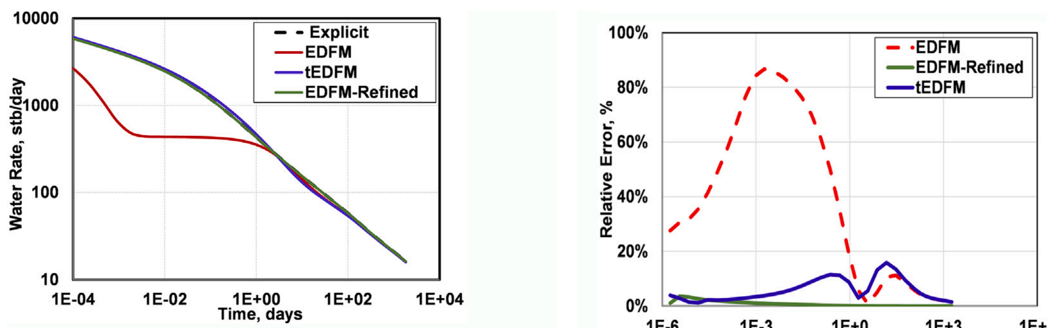

(a) The comparison of water rate from all four models.

(b) Relative Error

Fig. 2. The left image shows the comparison of water rate from the different approaches, whereas the right image shows their relative percentage errors. These results demonstrate that the proposed tEDFM approach matches the reference solution without mesh refinement.

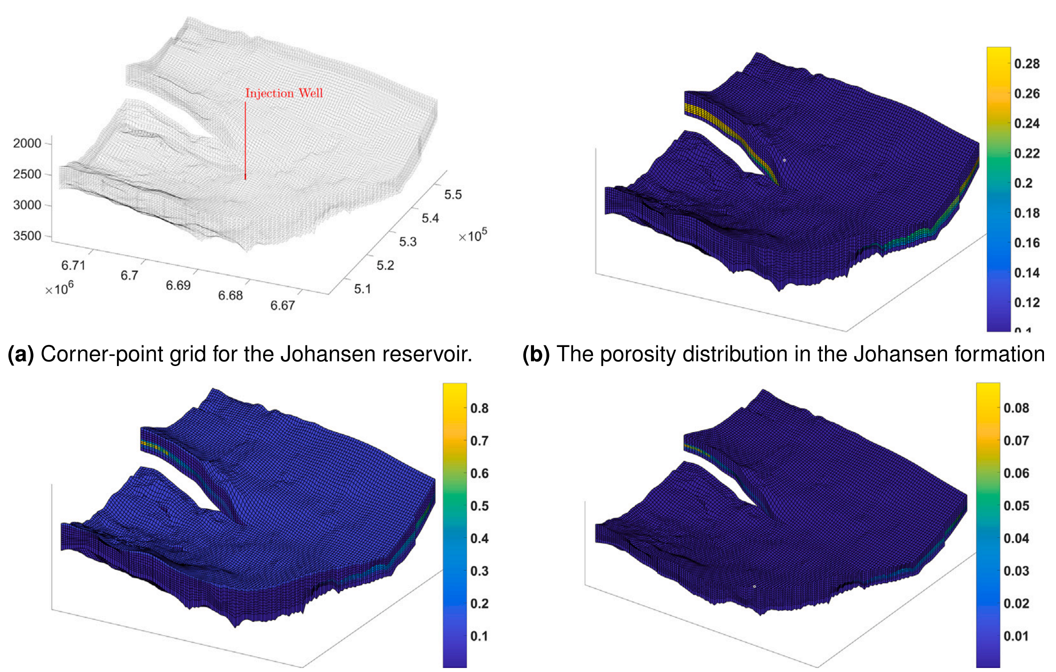

(c) Horizontal Permeability in Darcy

(d) Vertical Permeability in Darcy

Fig. 3. Profile of the permeability in the (c) x-direction and (d) z-direction. The location of the CO_2 injection well is shown in red.

storage. We multiplied the permeability of all cells in this layer by a factor of 10,000 so that the average permeability of this layer was of the same magnitude as the sand layers in layers 6 to 11. Without this increase in permeability, the leaked CO_2 would not enter into the top layer, which initially had a very low value of horizontal permeability. The CO_2 volume that leaked into the topmost layer was estimated by multiplying its pore volume by its CO_2 gas saturation and converting it to standard conditions.

Table 2
Reservoir model parameters for the Johansen case study.

Reservoir parameters	Value	Unit
Injection rate, q_{inj}	5,127,400	m^3/day
Reference pressure, P_{ref}	30×10^6	Pa
Reference temperature, T_{ref}	367.15	K
Reference fluid viscosity μ_{ref}	$[8 \times 10^{-4}, 5.68 \times 10^{-5}]$	Pa s
Reference fluid density ρ_{ref}	[1000, 686.5]	kg/m^3
Residual water saturation	0.27	–
Residual CO_2 saturation	0.2	–

We simulated CO_2 injection into the Johansen reservoir at a constant rate for 100 years, after which the migration of the CO_2 plume is observed for 1000 years. Fig. 4(a) and (b) compare our saturation profile to that from a commercial compositional simulator. The results show a good match in terms of the relative location of the CO_2 plume after 1100 years. Fig. 4(d) compares our simulated bottomhole pressure (BHP) values to the corresponding values from a commercial simulator. The results show a maximum error of 5%. Fig. 4(d) compares the amount of CO_2 leaked into the topmost layer of both simulators. The results indicate an almost identical breakthrough time, but the amount of CO_2 leaked into the topmost layer of our model is 12% more than the corresponding amount from the commercial simulator. These discrepancies can be attributed to the fundamental differences in the simulation models. We used a two-phase water-gas black-oil model, whereas the commercial simulator used a compositional approach that included a trace amount of methane for numerical stability.

4. Applications of tEDFM-CPG in modeling flow in fractured/Faulted reservoirs

Having verified the tEDFM-CPG model developed, the rest of this paper focuses on its application in studying the flow of CO_2 in reservoirs with fractures or faults in the storage rocks and caprocks. The first case study in this section focuses on the migration of CO_2 through a fractured caprock in a simple synthetic reservoir, whereas all other cases are based on the Johansen reservoir model presented in the previous section.

4.1. CO_2 leakage through naturally fractured caprocks

Subsurface rocks are typically naturally fractured to some extent (Gale et al., 2014; Shafiei et al., 2018). Therefore, it is essential to accurately model CO_2 flow in faulted/fractured rocks to reliably assess the risks of CO_2 leakage during long-term underground CO_2 storage. Considering that there is no technology available to determine the location, size, and other properties of all the fractures in the subsurface, we will generate a few stochastic fractures in the simple corner-point grid shown in Fig. 5(a). This simple domain consists of two storage rocks separated by the two blue layers of caprock in Fig. 5(a). For reference, we first simulated CO_2 injection into the "unfractured" reservoir for 20 years. The CO_2 is injected into the middle of the lower storage rock via the injector well shown as a red vertical line. Constant hydrostatic pressure was applied on all the sides of the reservoir, and the other model parameters are summarized in Table 3. The simulation results indicate that the injected supercritical CO_2 rises upward due to buoyancy and gets trapped beneath the caprock, as shown by the red cells in Fig. 5(b).

To account for the uncertainties in the size, location, and orientations of fractures that could exist in the caprock, we generated

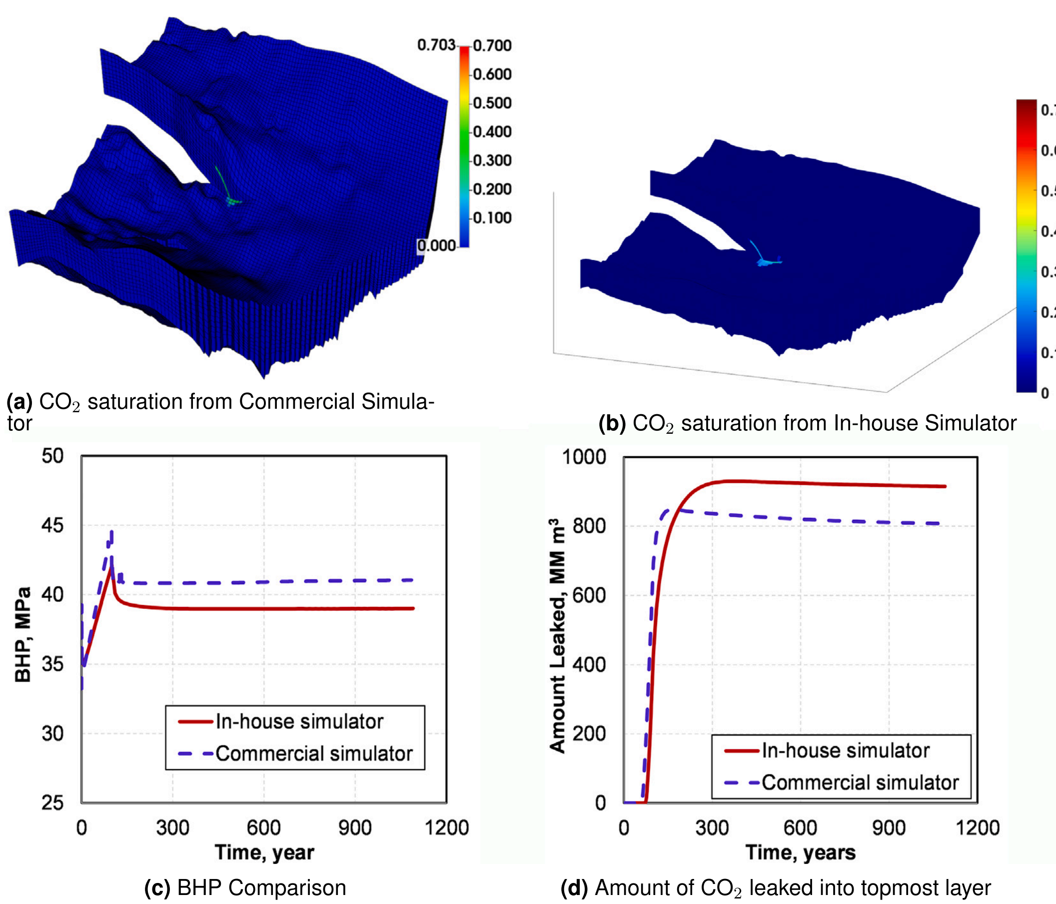

Fig. 4. The saturation profiles (after 1100 years) from (a) our in-house simulation match (b) the saturation profiles from a commercial compositional simulator. The line plots in (c) show a good match of the flowing bottomhole pressure (BHP), whereas (d) shows a comparison of the amount of CO_2 leaked into the topmost layer.

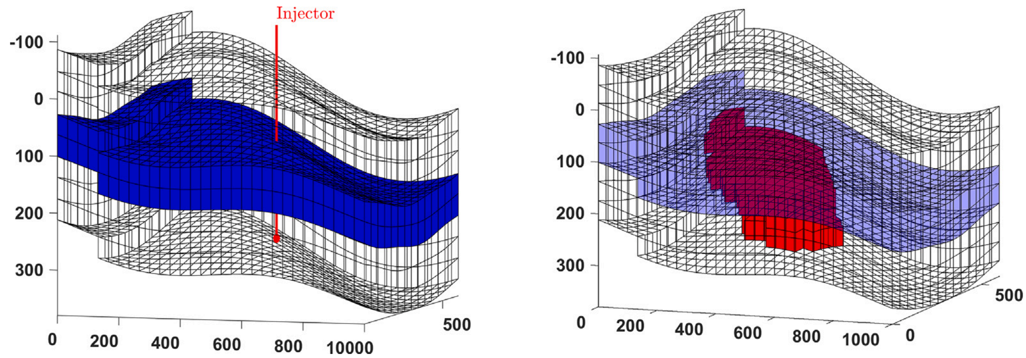

(a) Simulation domain with no NF **(b)** CO_2 plume

Fig. 5. Left image shows the simulation domain with no natural fracture in the cap rock, whereas the right figure shows the CO_2 plume after 20 years of injection.

Table 3
Reservoir model parameters for the natural fracture leakage case.

Reservoir parameters	Value	Unit
Reservoir dimension	[1000 600 300]	m
Fracture permeability, k_f	[100 100 10]	D
Fracture porosity, ϕ_f	0.5	–
Matrix permeability, k_m	[2 2 0.2]	D
Seal rock permeability, k_s	[2 2 0.2]	μD
Matrix porosity, ϕ_m	0.36	–
Injection rate, q_{inj}	0.0153	m^3/s
Initial saturation S_0	[1, 0]	–
Reference pressure, P_{ref}	15×10^6	Pa
Reference temperature, T_{ref}	305.15	K
Reference fluid viscosity μ_{ref}	$[8 \times 10^{-4}, 7.7 \times 10^{-5}]$	Pa s
Reference fluid density ρ_{ref}	[1000, 834.5]	kg/m^3
Minimum NF size	15	m
Average NF size	40	m
Maximum NF size	120	m
Residual water saturation	0.27	–
Residual CO_2 saturation	0.08	–

several stochastic fracture networks using the open-source Alghalandis Discrete Fracture Network Engineering (ADFNE) package Alghalandis (2018). We modified ADFNE to include the Power-law distribution to enable stochastic fracture modeling, and used this instead of the default exponential function. The size, location, and orientation of all fractures modeled in this work follow the Power-law, Poisson, and Fisher distributions, respectively.

A rigorous study of the fracture percolation threshold was conducted for this naturally fractured synthetic reservoir. For further details on the percolation threshold equations and computational procedure, the reader is referred to Amer and Olorode (2022). We simulated five different realizations of the system with 8, 16, 32, 64, 128, 256, and 512 natural fractures in the caprock. Therefore, the total number of fractured systems simulated was 35. Each realization was generated by modifying the "seed" provided as input to the stochastic fracture model. Fig. 6 shows one of the five realizations for four of the seven naturally fractured systems studied. These images show an increasing number of natural fractures, as expected.

Fig. 7 presents box plots and line plots that summarize our analysis of the fracture network connectivity for this synthetic fractured reservoir. The box plots were obtained from the five realizations of each number of fractures, whereas the line plots show the mean of the five realizations of each case. The Connectivity Index (CI) is defined as the ratio of the total number of fracture-fracture intersections in the reservoir domain to the total number of fractures in the reservoir. To render zero CI values meaningfully on the log-log box plot, we plotted them as 1×10^{-5}. The results indicate that there is essentially no connectivity between the two storage reservoirs when fewer than 32 natural fractures are present. When there are 64 fractures or more, the Figure shows finite values of fracture conductivity. Therefore, based on the CI values, the percolation threshold lies in the interval between 32 and 64 fractures.

We simulated CO_2 injection for 20 years, as in Fig. 5, and computed the amount of CO_2 that leaks into the shallower storage rock. The results also indicate that the percolation threshold is between 32 and 64 fractures. Fig. 8 presents the corresponding position of the CO_2 plume for the four fractured reservoir cases in Fig. 6. The results indicate that the natural fractures allow the injected CO_2 to leak through the caprock when there are more than 64 fractures in the caprock. Additionally, the results presented in Fig. 8 show that the amount of CO_2 leakage increases as the number of natural fractures in the caprock increases. Therefore, it is essential to conduct fracture connectivity analysis or completely avoid caprocks with natural fractures when selecting candidate deep saline aquifers for CO_2 injection.

4.2. Simulation of long-term CO_2 injection in fractured saline aquifers

Unlike all other Johansen cases in this work, this subsection ignores the top five shale layers of the formation, as in most published numerical studies of this field. The idea is to improve computational efficiency while observing the influence of fractures and their orientation on the CO_2 plume migration. Here, we introduce stochastic fracture networks into the reservoir and compare the CO_2 migration for this case to the original case presented without natural fractures in Fig. 4. Fig. 9 presents the simulation domain with (Fig. 9(b)) and without (Fig. 9(a)) natural fractures. In contrast, Fig. 9(c) shows the gas and water relative permeability curves used in the matrix and fracture cells. The number and orientation of the natural fractures introduced into the model are summarized using the Stereonet shown in Fig. 9(d). As discussed in the previous section, these natural fractures were generated using ADFNE. We also applied a constant hydrostatic pressure constraint on all sides of the simulation domain. We simulated a constant rate of CO_2 injection of 5,127,400 m^3/day for 100 years and simulated the system for another 1000 years after shutting in the well. The horizontal and vertical fracture permeability values were 100 and 10 Darcy, and a fracture porosity of 0.5 was used to account for the presence of cementation materials in the natural fractures.

After simulating the system for a total of 1100 years, we generated the plots of the CO_2 plume for the cases with and without natural fractures. The top row of Fig. 10 presents the simulation results for the case with no natural fractures at the specified output times. Similarly, the bottom row presents the corresponding results for the case with natural fractures. Examining these profiles reveals that CO_2 continues migrating toward the shallower layers of the reservoir even after the CO_2 injection

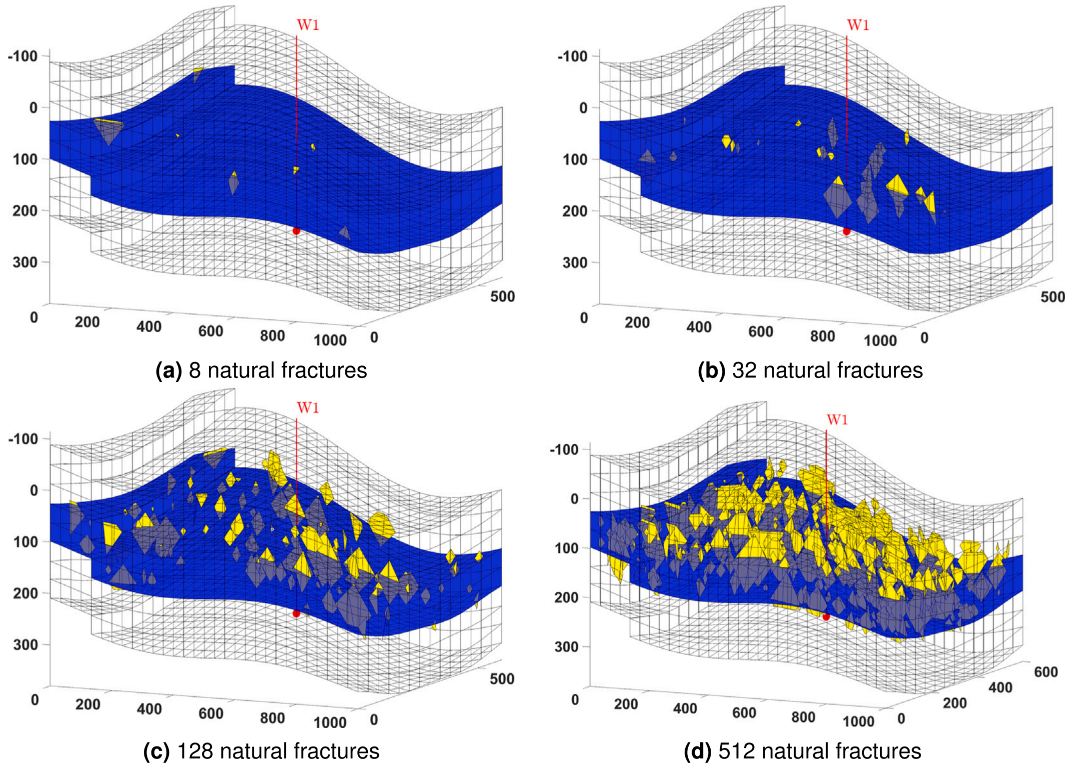

Fig. 6. These images show the numerical simulation domain for leakage analysis with different realizations of natural fractures.

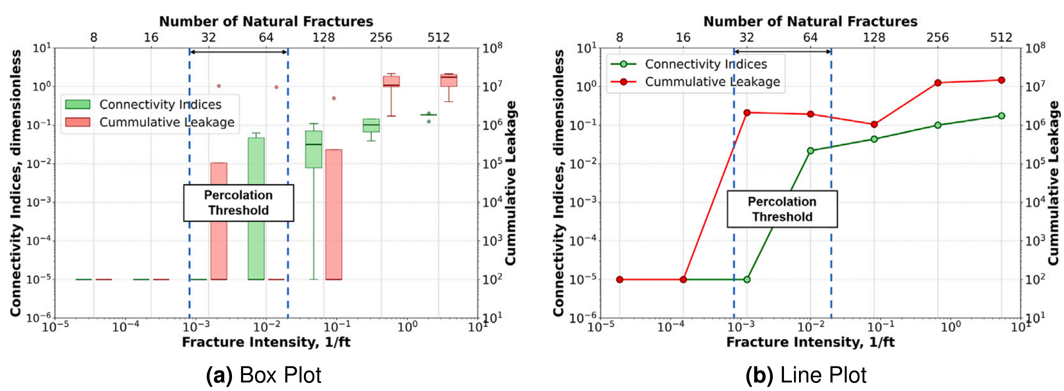

Fig. 7. Amount of leaked CO_2 increases when the percolation threshold is exceeded.

has stopped. In the presence of natural fractures, the migration rate is notably higher, with the CO_2 plume nearly reaching the reservoir boundary at the end of the simulation. The migration rate in a naturally fractured reservoir could be an essential factor to consider if freshwater aquifers are located above the deep saline aquifer into which CO_2 is to be injected. This is because the CO_2 could leak into the freshwater aquifer and contaminate this source of drinking water.

To quantify CO_2 migration in the reservoir, we selected a zone of investigation around the injection well. This zone is shown as the yellow cells in Fig. 11(a), and the cell the vertical well cuts through in this layer is shown in red. We computed the total amount of CO_2 in the yellow cells and plotted it against time in Fig. 11(b). The results show that the amount of CO_2 increased at the same rate during the injection period for the cases with and without natural fractures. However, the amount of CO_2 in the yellow cells declined more in the case with fractures during the post-injection period. This is because the injected CO_2 migrated more quickly up the structure and out of the zone of investigation in this case, as shown in Fig. 10.

4.3. Simulation of long-term CO_2 injection in faulted saline aquifers

Unlike the previous subsection, this subsection does not artificially introduce natural fractures into the Johansen formation. Instead, it focuses on understanding the effect of the faults in the Johansen reservoir on CO_2 migration and leakage. To this end, we extracted all the faults provided in the original simulation model from Equinor, as shown in Fig. 12(a). Of all the faults shown in Fig. 12(a), the large fault in the middle of the domain is the only one expected to play a significant role in the CO_2 migration. This is based on the previous Johansen simulation results presented. To accurately model this fault, we represent each of the two faces of the fault as fractures, as shown in blue in Fig. 12(b). This approach allows us to account for the expected flow along and across these fault surfaces using the tEDFM-CPG model presented in this work. The red vertical line in this figure represents the CO_2 injection well. Fig. 3(b)–(d) present the horizontal permeability, vertical permeability, and porosity distributions of the full Johansen model. These three-dimensional profiles of permeability and porosity show that the

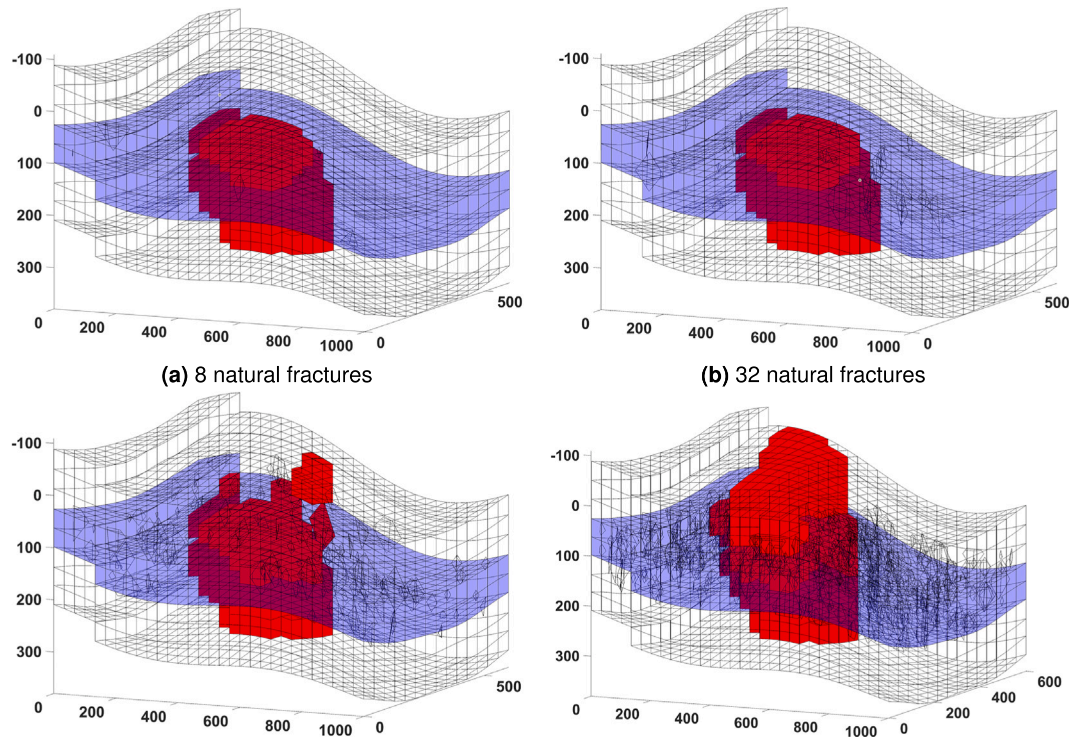

(a) 8 natural fractures

(b) 32 natural fractures

(c) 128 natural fractures

(d) 512 natural fractures

Fig. 8. These images show the CO_2 plume profile for the cases presented in Fig. 6 after 20 years of CO_2 injection.

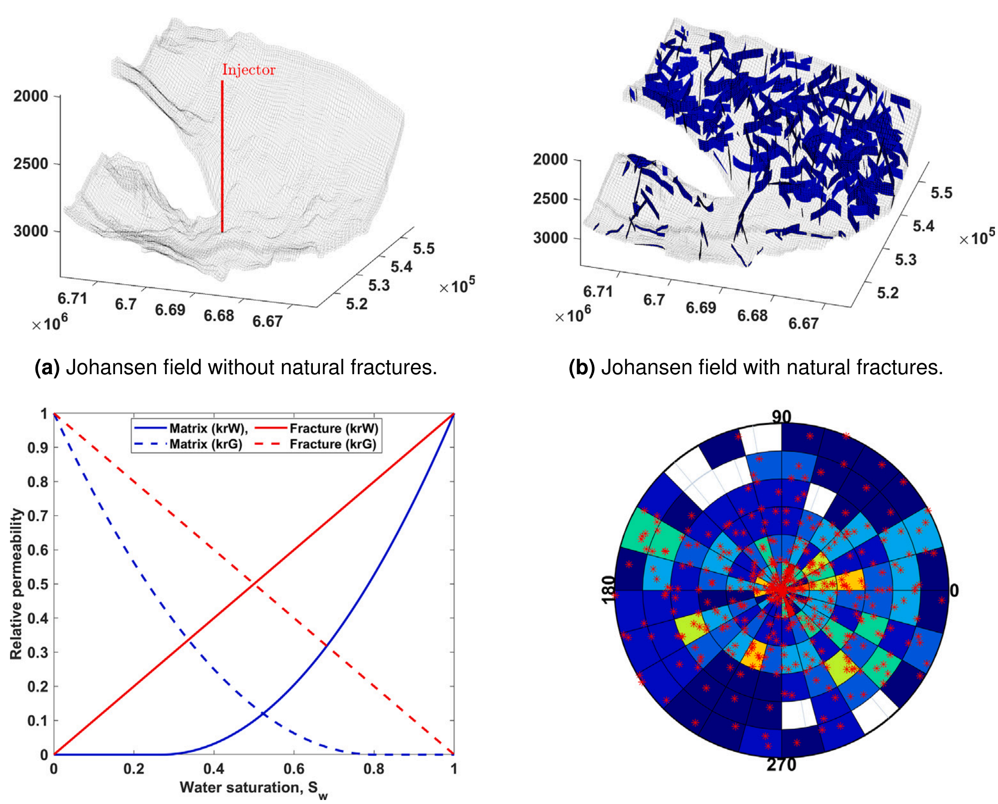

(a) Johansen field without natural fractures.

(b) Johansen field with natural fractures.

(c) Relative permeability curves.

(d) Natural Fracture Orientations.

Fig. 9. Simulation model developed with natural fractures in the Johansen formation.

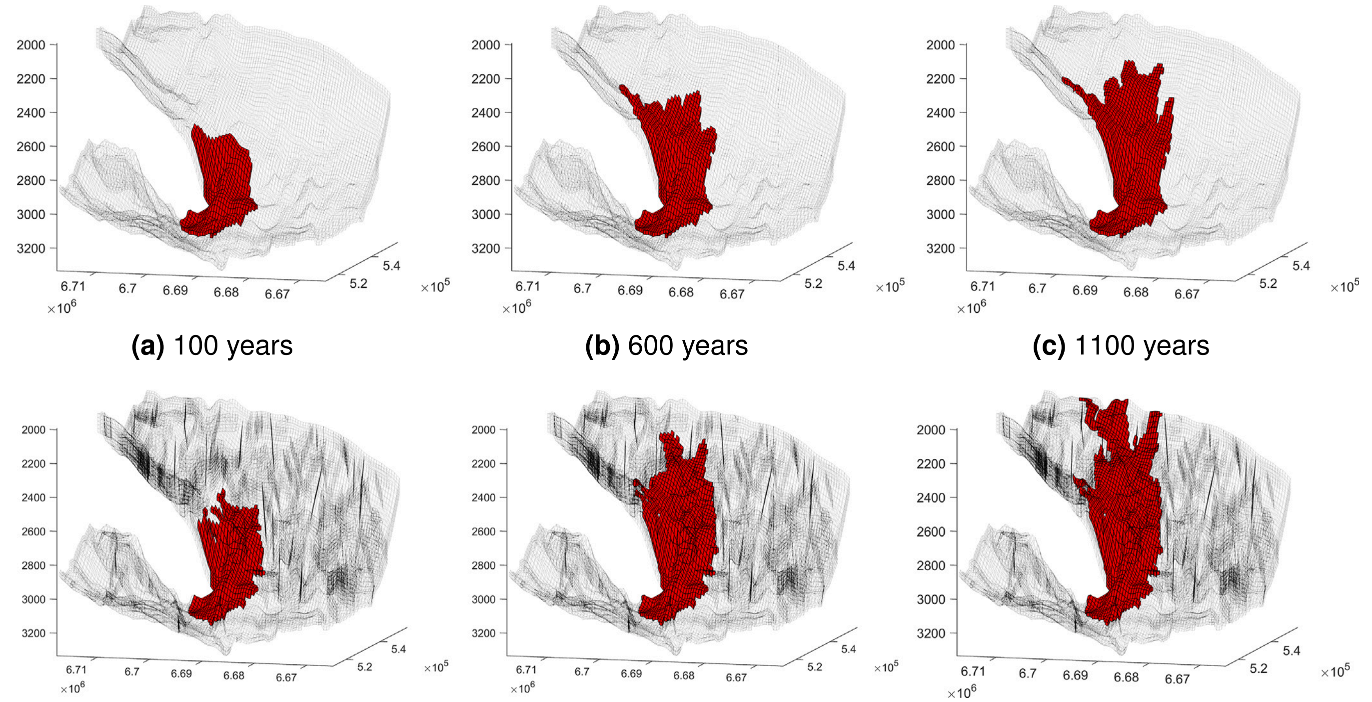

(a) 100 years **(b)** 600 years **(c)** 1100 years

(d) 100 years **(e)** 600 years **(f)** 1100 years

Fig. 10. Evolution of CO_2 plume in the Johansen formation with and without natural fractures. The top row corresponds to the case with no natural fractures, whereas the bottom row shows the corresponding naturally fractured cases.

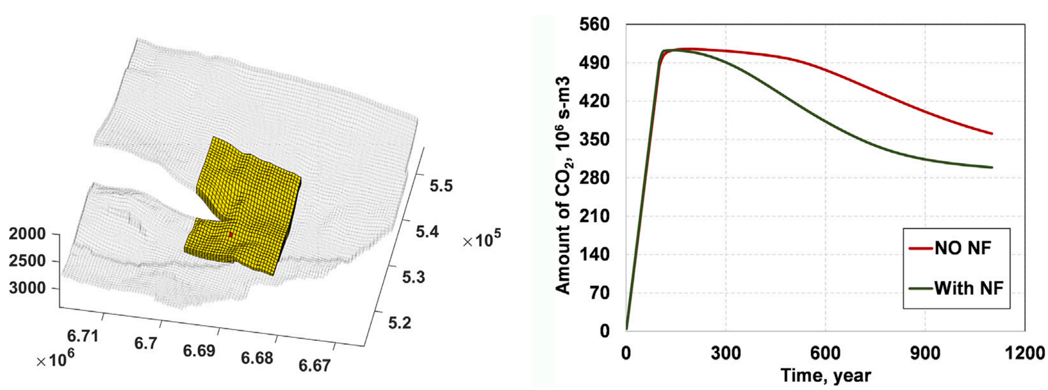

(a) Zone of investigation **(b)** Amount of CO_2 in the yellow zone.

Fig. 11. Left image shows the zone of investigation marked in yellow and the well cell marked in red. The right image shows the evolution of the total amount of CO_2 in the investigation zone over time.

first five layers have much lower permeability and porosity than the deeper layers shown in yellow colors. It is worth clarifying that the low-permeability regions southwest of layers 6 through 11 were also filtered in the subdomain of the Johansen model presented in Fig. 3.

The standard approach to account for faults in petroleum reservoirs involves scaling the transmissibility across the matrix faces parallel to the fault surface. For conductive faults, a fault transmissibility multiplier greater than one is used to increase the flow rate across the pair of matrix cells that share the matrix face parallel to the fault surface. In contrast, low-conductivity faults are modeled using transmissibility multipliers less than one. There are two errors implicit in this approach–(a) it does not account for the flow in the two directions parallel to the fault surface because only the flow orthogonal to the fault surface is modified, and (b) it does not account for the fact that faults typically have a finite volume associated with the damage zone near the fault surface. Fault-damaged zones also have deformation bands, which are zones where the rock has been deformed due to localized stresses. These bands can significantly impact fluid flow, potentially sealing or reducing flow along the fault. Using tEDFM-CPG allows us to represent the damage zone's petrophysical properties (porosity and permeability) with the fault/fracture cell properties.

Commercial geoscience packages typically use pillar gridding to model the structure of faulted 3D reservoirs and generate corner-point grids. Some of the cells in these grids are very small because they are truncated against fault planes. Thus, robust reservoir simulators typically remove these small cells to facilitate numerical convergence. They also account for the flow across the fault planes after removing these small cells. Both objectives are achieved using specific keywords (Pettersen, 2006). Our simulation uses the corner-point grid-processing functionality provided in MRST to achieve this. However, we replaced

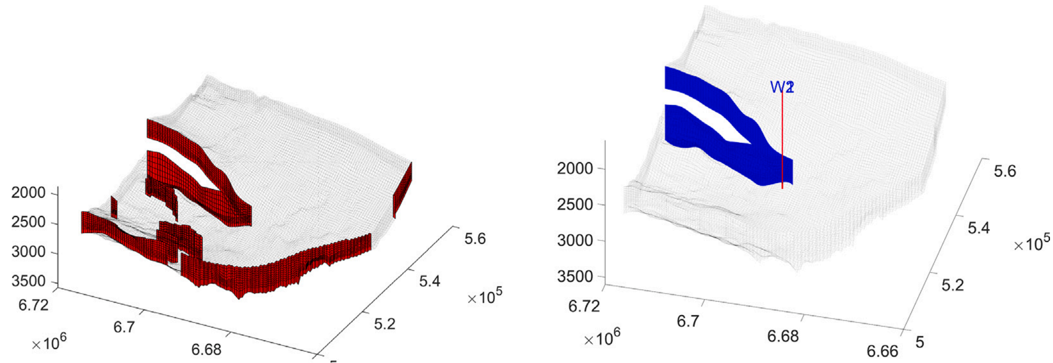

(a) All faults in the Johansen formation **(b)** Two faces of the fault of interest

Fig. 12. Images illustrate (a) all the faults in the Johansen model, (b) a representation of the large fault surfaces with intersecting fracture planes. The red vertical line in (b) represents the CO_2 injection well.

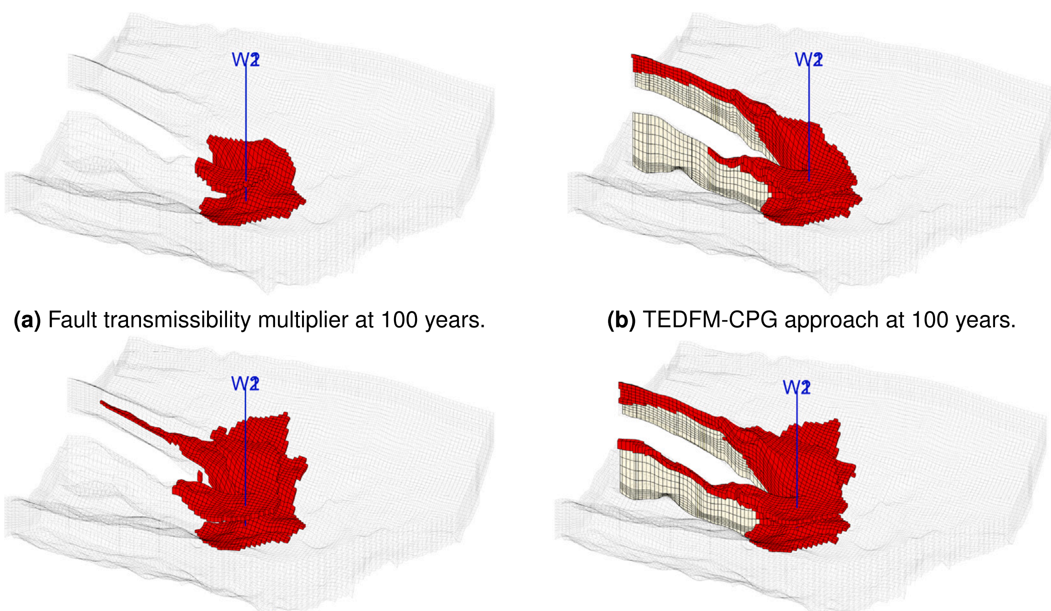

(a) Fault transmissibility multiplier at 100 years. **(b)** TEDFM-CPG approach at 100 years.

(c) Fault transmissibility multiplier at 1100 yrs. **(d)** TEDFM-CPG approach at 1100 years

Fig. 13. The results show the CO_2 plume for the fault transmissibility multiplier and tEDFM-CPG approaches at the end of injection (100 years) and at the end of the simulation (1100 years). The red cells are the cells with a CO_2 saturation over 1e-4.

the standard fault transmissibility multiplier with a more robust tEDFM-CPG model that allows us to account for flow across faults in addition to the flow along the faults.

To demonstrate the importance of accounting for the flow along and across faults, we used both the fault transmissibility multiplier and the tEDFM-CPG approaches to simulate CO_2 injection into the reservoir with the two fault surfaces in Fig. 12(b). The model parameters and operating conditions are identical to those presented in the previous subsection for the case without natural fractures. To ensure a reasonable comparison between these two approaches, we modeled the fault transmissibility multiplier case by multiplying the transmissibility across the fault faces by a factor. This factor was obtained by dividing the fracture's permeability in the x-direction by the average x-directional permeability (K_x) of the matrix cells on either side of the fault planes.

As in all other Johansen cases simulated (with the exception of the fractured Johansen reservoir case, which considered only the permeable, bottom six layers), the results shown in this subsection are based on the full model with all 11 layers. This allows us to quantify the CO_2 leakage from these six sand layers into the top five shale layers of caprock. Fig. 13(a) and (b) show the CO_2 plume corresponding to the fault transmissibility multiplier and tEDFM-CPG approaches after 100 years of CO_2 injection. The results show that the upward CO_2 plume migration is limited when the flow in the directions parallel to the fault surfaces is not considered, as in the conventional fault transmissibility multiplier approach. In contrast, when we use tEDFM-CPG to account for flow along and across the fault surface, the CO_2 plume migration is much faster. Furthermore, Fig. 13(c) and (d) show the CO_2 plume after 1100 years. A comparison of these two figures shows that the amount of CO_2 leaked into the topmost five layers is much lower when only the flow across faults is modeled (using the fault multiplier approach) than when tEDFM-CPG is used to account for flow along and across the faults. This observation was also confirmed by visualizing the CO_2 plume layer-by-layer.

To facilitate the observation of how the CO_2 gas saturation evolves in the entire simulation domain without layer-by-layer visualization or taking multiple cross sections, we leveraged a robust mixed reality (MR) visualization workflow we developed for any grid system. However, considering that corner-point grids are the standard grids used to represent

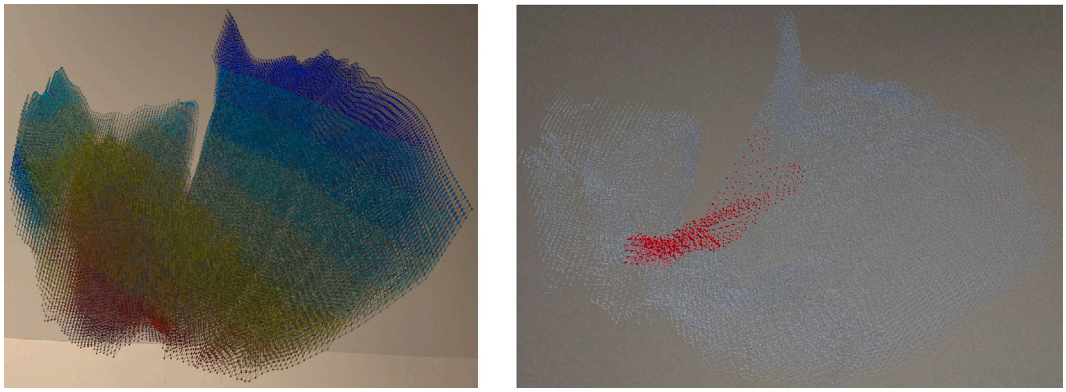

(a) MR screenshot of pressure profile. **(b)** MR screenshot of CO_2 plume.

Fig. 14. The MR screenshots show (a) the pressure and (b) the CO_2 plume profiles at the end of the simulation of the fault-multiplier case. The red spheres in the CO_2 plume profile indicate cells with CO_2 gas saturation over 1e-4, whereas other cells are represented with gray, partially transparent spheres.

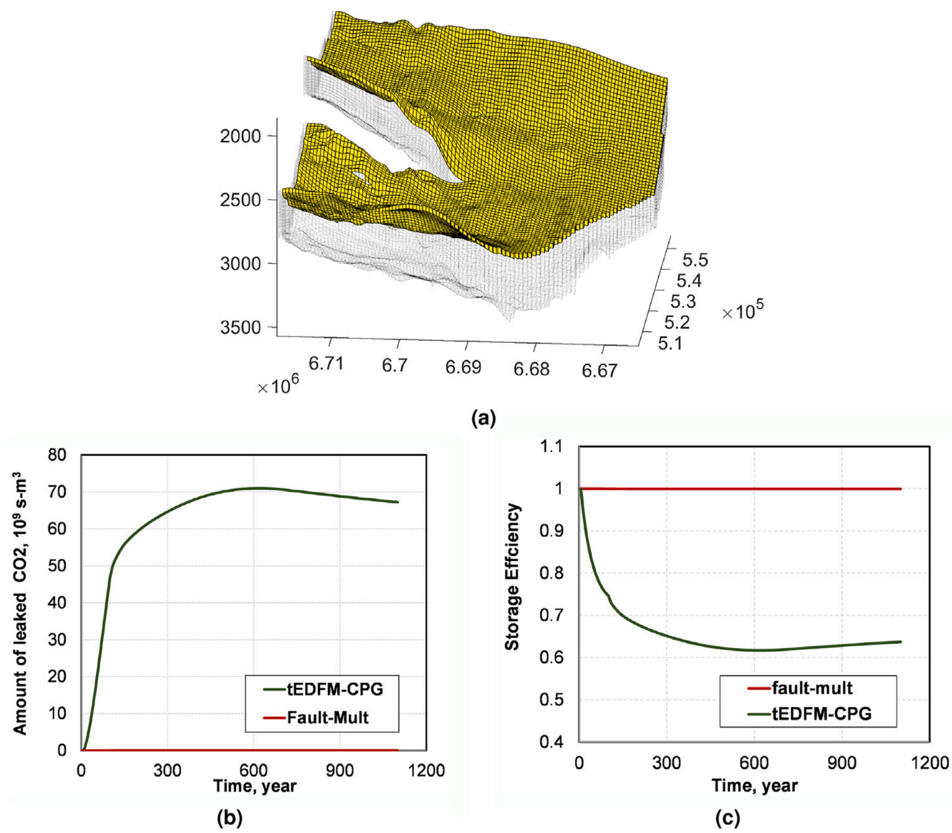

Fig. 15. This figure presents (a) the top layer of the Johansen layer in yellow, (b) a comparison of the total amount of CO_2 leaked into the top layer, and (c) a comparison of the storage efficiency from the fault-multiplier and tEDFM-CPG models.

geological reservoirs, this section only focuses on visualizing physical variables on corner-point grids. The general idea involves representing a corner-point grid as a graph and using colored spherical glyphs to represent the magnitude of the physical quantities plotted at each cell's centroid. Figs. 14(a) and (b) present MR screenshots of the pressure and CO_2 plume after 1100 years. Both images are based on the results from the fault transmissibility multiplier approach. Warmer colors in the pressure profile indicate higher magnitudes of the pressure. In contrast, the red spheres in the CO_2 plume profile indicate cells with a CO_2 gas saturation over 1e-4. The other cells with lower gas saturation are shown as partially transparent gray spheres. To ensure that the connectivity between cells in the simulation is maintained without clogging up the MR environment, we connected these spheres to neighboring cells using thin gray lines. This allows the user to see through the domain while walking around or zooming in on any region of the simulation domain. The videos provided at https://youtube.com/shorts/kQa4lRjxNnM and https://youtube.com/shorts/R2ljJW0py6c present the MR representation of the pressure and CO_2 gas plume profiles of the Johansen model with the fault multiplier after 1100 years. The videos and screenshots from the MR headsets are inadequate at representing the fully 3D and immersive interaction in the MR environment because they project the 3D environment onto 2D screens.

To simulate the potential CO_2 leakage through the faults into shallower formations, we increased the horizontal permeability of the topmost shale layer. Thus, the topmost layer shown in Fig. 15 mimics more permeable shallower sands above the target reservoir sand for CO_2 storage. We multiplied the permeability of all cells in this layer by a factor of 10,000 so that the average permeability of this layer was of the same magnitude as the sand layers in layers 6 to 11. Without this increase in permeability, the leaked CO_2 would not enter into the top layer, which initially had a very low value of horizontal permeability. The CO_2 volume that leaked into the topmost layer was estimated by multiplying its pore volume by its CO_2 gas saturation and converting it to standard conditions. Although the Johansen formation has a thick caprock, the results presented in this subsection clearly show that the fault running through the caprock can easily compromise its sealing potential. This is because the migration of the CO_2 can be accelerated by the upward flow along the fault (or its damage zone), which is implicitly missing when fault transmissibility multipliers are used in standard reservoir simulators. It is worth noting that this is a significant environmental concern to avoid because CO_2 leakage along faults can contaminate shallower freshwater aquifers, which serve as drinking water sources.

Fig. 15(b) and (c) show the amount of CO_2 leaked at the topmost layer and the storage efficiency at the end of the simulation respectively. From the results, we observe a significant amount of CO_2 leaked from the topmost layer when we account for both the flow along and across faults. Also, we observe lower storage efficiency of the topmost layer due to the increased flow when the flow along is accounted for as in the tEDFM-CPG case. This behavior can have implications for predicting long-term plume migration and the stability of the formation.

Our performance studies indicate that the tEDFM-CPG model runs for twice the duration of the fault-transmissibility multiplier approach. This is reasonable considering the increased accuracy achieved by introducing fracture cells to model the flow along faults.

5. Conclusions

This work involves the development of a transient embedded discrete fracture model for corner-point grids (tEDFM-CPG), which was used to study CO_2 leakage through faulted or fractured reservoirs or cap rocks. The conclusions based on the cases studied can be summarized as follows:

- The proposed tEDFM-CPG can accurately and efficiently model transient flow in corner-point grids.
- The simulation results show that using tEDFM-CPG to model flow along and across faults addresses the common error introduced by modeling only flow across faults with fault transmissibility multipliers.
- The tEDFM-CPG simulation of CO_2 storage in the Johansen formation indicates that natural fractures or damage zones near faults can significantly increase CO_2 leakage through cap rocks.
- The field-scale simulation results indicate that the amount and rate of CO_2 leakage increase with an increase in the number of conductive natural fractures.
- The visualization of the simulation results in mixed reality (MR) indicates that this technology can facilitate the observation of the migration path of the injected CO_2 in deep saline aquifers.

Although tEDFM-CPG improves accuracy and efficiency in modeling CO_2 flow through faults and fractures, several limitations remain. First, using corner-point grids provides the flexibility of modeling real field-scale geological models, but their creation from pillar gridding could yield small and irregular cells near faults. Second, while the model is valid across a wide range of fracture/fault and matrix permeabilities, at extremely low fracture/fault permeability values, tEDFM-CPG inherits the standard EDFM limitation of not fully capturing their sealing properties. Addressing this would require developing a projection-based formulation for corner-point grids (pEDFM-CPG), which can be a future extension of this work.

In conclusion, this study underscores the limitations of conventional modeling tools in evaluating the feasibility of potential CO_2 storage sites and introduces a more reliable and efficient framework to support safer large-scale CO_2 storage projects. The ability of the proposed model to efficiently quantify flow along and across faults in caprocks (Fitts and Peters, 2013) is critical for designing effective pressure management strategies (Rashid et al., 2025), protecting shallow aquifers (Esposito and Benson, 2011), and ensuring the long-term security of geologic CO_2 storage at the field scale.

CRediT authorship contribution statement

H.U. Rashid: Writing – original draft, Visualization, Validation, Methodology, Investigation, Formal analysis, Data curation. **C.S. Igweonu:** Writing – original draft, Visualization, Validation, Investigation, Formal analysis, Data curation. **O.M. Olorode:** Writing – review & editing, Writing – original draft, Supervision, Software, Resources, Project administration, Methodology, Investigation, Funding acquisition, Conceptualization. **A.A. Abdullah:** Visualization. **F. Olalotiti:** Writing – review & editing.

Declaration of competing interest

The authors declare that they have no known competing financial interests or personal relationships that could have appeared to influence the work reported in this paper.

Acknowledgements

The work of O.O., C.I., and A.A. was supported by the U.S. Department of Energy, Office of Science, Office of Basic Energy Sciences, Geosciences Program under Award Number DE-SC0024382.

Appendix A. Modeling conductive faults with tEDFM in corner-point grids

This section shows the importance of modeling flow along fractures (parallel to the fracture surface) using a carefully designed simulation study. Most simulators overlook flow along faults and only adjust transmissibility across (or orthogonal) to the fault surface. This is achieved by multiplying the fault transmissibility (in the direction orthogonal to the fracture surface) by a finite value. Therefore, this approach is loosely referred to as the “fault-multiplier” approach. The omission of the flow in the direction parallel to the fracture plane can result in substantial reservoir modeling and forecasting errors, especially when the fault is highly conductive and connected to an aquifer. Water breakthroughs can occur much earlier than expected if we do not correctly account for flow along a conductive fault. To this end, we created the simulation domain outlined in Fig. A.1. Table A.1 details the reservoir parameters used in this simulation.

Fig. A.2 presents the saturation profile at the end of the simulation. The low water saturation observed at the reservoir top from the fault-multiplier approach is attributable to the lack of modeling of vertical water flow through the conductive fault. The saturation profile from tEDFM-CPG closely matches the reference solution. This observation shows that modeling flow across a fault without accounting for flow along the fault will underestimate water production. Additionally, Fig. A.3 compares water rates in the producer. All models accurately predict water breakthrough when considering both flows along and across the fault, but the injected water never breaks through to the production well in the fault-multiplier approach. These results confirm the need to account for flow along and across faults and fractures in subsurface reservoirs.

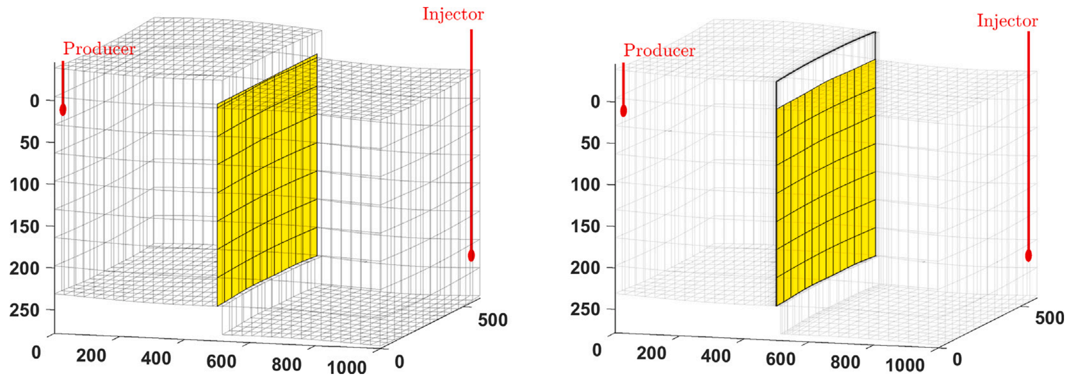

(a) Cartesian grid. **(b)** Refined grid

Fig. A.1. Simulation domain for a simple faulted system. The left figure shows the unrefined corner-point grid, whereas the right figure shows a locally refined corner-point grid.

Table A.1
Reservoir model parameters for the simple faulted system.

Reservoir parameters	Value	Unit
Reservoir dimension	[1000 600 270]	m
Initial reservoir pressure, P_i	5000	psi
Wellbore flowing pressure, P_{wf}	1000 psi	psi
Fracture half-length, x_f	300	m
Fracture height, h_f	270	m
Fracture width, w_f	0.01	ft
Fracture permeability, k_f	[1000 1000 1000]	D
Fracture porosity, ϕ_f	0.5	–
Matrix permeability, k_m	[100 100 10]	mD
Matrix porosity, ϕ_m	0.16	–
Well radius, r_w	0.32	ft
Injection rate, q_{inj}	0.01	m^3/day
Initial saturation S_0	$[0, 1, 0]$	–

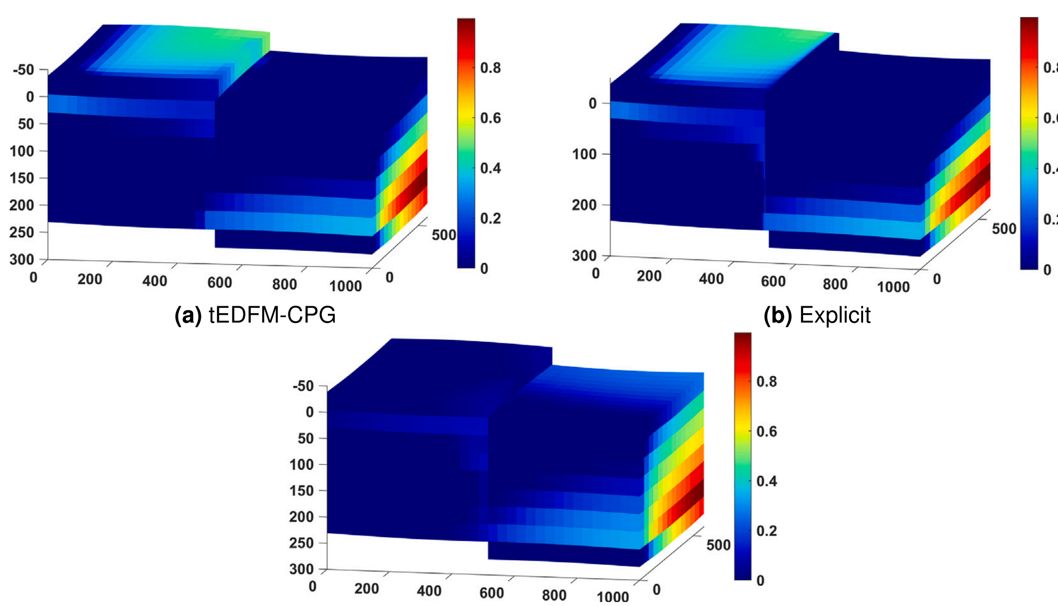

(a) tEDFM-CPG **(b)** Explicit **(c)** Fault Multiplier

Fig. A.2. Water saturation profile at the end of simulation shows a reasonable match between tEDFM-CPG and the reference solution, whereas the fault-multiplier approach shows lower water saturation near the producer.

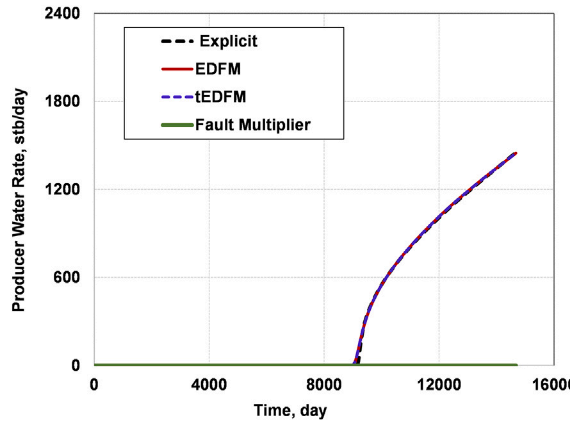

Fig. A.3. Lack of water production from the fault multiplier approach indicates that it severely underestimates the water production in comparison to the reference solution (explicit model). In contrast, the proposed tEDFM-CPG approach matches the reference solution.

Data availability

Data will be made available on request.

References

Alghalandis, Y.F., 2018. DFNE Practices with ADFNE. Alghalandis Computing, Toronto, ON Canada.
Amer, H., Olorode, O., 2022. Numerical evaluation of a novel slot-drill enhanced oil recovery technology for tight rocks. SPE J. 1–24.
Azom, P.N., Javadpour, F., 2012. Dual-continuum modeling of shale and tight gas reservoirs. In: SPE Annual Technical Conference and Exhibition in San Antonio, Texas, SPE–159584. SPE.
Bachu, S., 2002. Sequestration of co2 in geological media in response to climate change: road map for site selection using the transform of the geological space into the co2 phase space. Energy Convers. Manag. 43 (1), 87–102.
Bell, I.H., Wronski, J., Quoilin, S., Lemort, V., 2014. Pure and pseudo-pure fluid thermophysical property evaluation and the open-source thermophysical property library Coolprop. Ind. Eng. Chem. Res. 53 (6), 2498–2508.
Benson, S.M., Cole, D.R., 2008. Co2 sequestration in deep sedimentary formations. Elements 4 (5), 325–331.
Bentham, M., Kirby, M., 2005. Co2 storage in saline aquifers. Oil Gas Sci. Technol. 60 (3), 559–567.
Bryant, S.L., Lakshminarasimhan, S., Pope, G.A., 2008. Buoyancy-dominated multiphase flow and its effect on geological sequestration of co2. SPE J. 13 (4), 447–454.
Cavanagh, A.J., Haszeldine, R.S., 2014. The Sleipner storage site: capillary flow modeling of a layered co2 plume requires fractured shale barriers within the Utsira formation. Int. J. Greenh. Gas Control 21, 101–112.
Dai, Z., Xu, L., Xiao, T., McPherson, B., Zhang, X., Zheng, L., Dong, S., Yang, Z., Soltanian, M.R., Yang, C., et al., 2020. Reactive chemical transport simulations of geologic carbon sequestration: methods and applications. Earth-Sci. Rev. 208, 103265.
Ding, Y., Lemonnier, P., 1995. Use of corner point geometry in reservoir simulation. In: SPE International Oil and Gas Conference and Exhibition in China, SPE–29933. SPE.
Eiken, O., Ringrose, P., Hermanrud, C., Nazarian, B., Torp, T.A., Høier, L., 2011. Lessons learned from 14 years of CCS operations: Sleipner, in Salah and snøhvit. Energy Procedia 4, 5541–5548.
Emami-Meybodi, H., Hassanzadeh, H., Green, C.P., Ennis-King, J., 2015. Convective dissolution of co2 in saline aquifers: progress in modeling and experiments. Int. J. Greenh. Gas Control 40, 238–266.
Esposito, A., Benson, S.M., 2011. Remediation of possible leakage from geologic co2 storage reservoirs into groundwater aquifers. Energy Procedia 4, 3216–3223.
Fisher, Q., Jolley, S., 2007. Treatment of faults in production simulation models. Struct. Complex Reserv. 292, 219–233.
Fitts, J.P., Peters, C.A., 2013. Caprock fracture dissolution and co2 leakage. Rev. Mineral. Geochem. 77 (1), 459–479.
Gale, J.F., Laubach, S.E., Olson, J.E., Eichhubl, P., Fall, A., 2014. Natural fractures in shale: a review and new observations. AAPG Bull. 98 (11), 2165–2216.
Gunter, W., Perkins, E., Hutcheon, I., 2000. Aquifer disposal of acid gases: modelling of water–rock reactions for trapping of acid wastes. Appl. Geochem. 15 (8), 1085–1095.
Hajibeygi, H., Karvounis, D., Jenny, P., 2011. A hierarchical fracture model for the iterative multiscale finite volume method. J. Comput. Phys. 230 (24), 8729–8743.
Ide, S.T., Jessen, K., Orr Jr, F.M., 2007. Storage of co2 in saline aquifers: effects of gravity, viscous, and capillary forces on amount and timing of trapping. Int. J. Greenh. Gas Control 1 (4), 481–491.
Jiang, L., Chen, Z., Ali, S.F., Zhang, J., Chen, Y., Chen, S., 2022. Storing carbon dioxide in deep unmineable coal seams for centuries following underground coal gasification. J. Clean. Prod. 378, 134565.
Krevor, S., De Coninck, H., Gasda, S.E., Ghaleigh, N.S., de Gooyert, V., Hajibeygi, H., Juanes, R., Neufeld, J., Roberts, J.J., Swennenhuis, F., 2023. Subsurface carbon dioxide and hydrogen storage for a sustainable energy future. Nat. Rev. Earth Environ. 4 (2), 102–118.
Laesecke, A., Muzny, C.D., 2017. Reference correlation for the viscosity of carbon dioxide. J. Phys. Chem. Ref. Data 46 (1).
Lee, S., Jensen, C., Lough, M., 2000. Efficient finite-difference model for flow in a reservoir with multiple length-scale fractures. SPE Journal 5 (3), 268–275.
Lee, S.H., Lough, M., Jensen, C., 2001. Hierarchical modeling of flow in naturally fractured formations with multiple length scales. Water Resour. Res. 37 (3), 443–455.
Li, L., Lee, S.H., et al., 2008. Efficient field-scale simulation of black oil in a naturally fractured reservoir through discrete fracture networks and homogenized media. SPE Reserv. Eval. & Eng., vol. 11. Society of Petroleum Engineers, pp. 750–758 (4).
Li, Z., Dong, M., Li, S., Huang, S., 2006. Co2 sequestration in depleted oil and gas reservoirs—caprock characterization and storage capacity. Energy Convers. Manag. 47 (11–12), 1372–1382.
Lie, K.-A., 2019. An Introduction to Reservoir Simulation Using MATLAB/GNU Octave: User Guide for the MATLAB Reservoir Simulation Toolbox (MRST). Cambridge University Press.
Manzocchi, T., Heath, A., Palananthakumar, B., Childs, C., Walsh, J., 2008. Faults in conventional flow simulation models: a consideration of representational assumptions and geological uncertainties. Pet. Geosci. 14 (1), 91–110.
Metz, B., Davidson, O., De Coninck, H., Loos, M., Meyer, L., 2005. IPCC Special Report on Carbon Dioxide Capture and Storage. Cambridge University Press, Cambridge.
Michael, K., Arnot, M., Cook, P., Ennis-King, J., Funnell, R., Kaldi, J., Kirste, D., Paterson, L., 2009. Co2 storage in saline aquifers I—current state of scientific knowledge. Energy Procedia 1(1), 3197–3204.
Moinfar, A., 2013. Development of an Efficient Embedded Discrete Fracture Model for 3D Compositional Reservoir Simulation in Fractured Reservoirs (Ph.D. thesis), The University of Texas at Austin.
Moinfar, A., Varavei, A., Sepehrnoori, K., Johns, R.T., et al., 2013. Development of a coupled dual continuum and discrete fracture model for the simulation of unconventional reservoirs. In: SPE Reservoir Simulation Symposium. Society of Petroleum Engineers.
Neufeld, J.A., Hesse, M.A., Riaz, A., Hallworth, M.A., Tchelepi, H.A., Huppert, H.E., 2010. Convective dissolution of carbon dioxide in saline aquifers. Geophys. Res. Lett. 37 (22).
Olorode, O., Rashid, H., 2022. Analytical modification of EDFM for transient flow in tight rocks. Sci. Rep. 12 (1), 22018.
Olorode, O., Wang, B., Rashid, H.U., et al., 2020. Three-Dimensional Projection-Based Embedded Discrete-Fracture Model for Compositional Simulation of Fractured Reservoirs SPE Journal. Publisher. Society of Petroleum Engineers.
Olorode, O.M., 2017. A New Multicontinuum Model for Compositional Gas Transport in a Deformable Shale Formation (Ph.D. thesis).
Pettersen, Ø., 2006. Basics of Reservoir Simulation with the Eclipse Reservoir Simulator, vol. 114. Lecture Notes. University of Bergen, Norway, p. 81.
Pruess, K., et al., 2005. Eco2n: a tough2 fluid property module for mixtures of water, NaCl. In: And CO_2, vol. 497. Lawrence Berkeley National Laboratory, Berkeley, CA.
Rao, X., Cheng, L., Cao, R., Jia, P., Dong, P., Du, X., 2019a. A modified embedded discrete fracture model to improve the simulation accuracy during early-time production of multi-stage fractured horizontal well. In: SPE/IATMI Asia Pacific Oil and Gas Conference and Exhibition, Bali, Indonesia, SPE–196263. SPE.
Rao, X., Cheng, L., Cao, R., Jia, P., Yonghui, W., He, Y., Chen, Y., 2019b. An efficient three-dimensional embedded discrete fracture model for production simulation of multi-stage fractured horizontal well. Eng. Anal. Bound. Elem. 106, 473–492.
Rashid, H., Olorode, O., Chukwudozie, C., 2022. An iteratively coupled model for flow, deformation, and fracture propagation in fractured unconventional reservoirs. J. Pet. Sci. Eng. 214, 110468.
Rashid, H.U., Olorode, O., 2024. A continuous projection-based EDFM model for flow in fractured reservoirs. SPE Journal 29 (1), 476–492.
Rashid, H.U., Pachalieva, A., O'Malley, D., Differentiable multiphase flow model for physics-informed machine learning in reservoir pressure management, arXiv preprint arXiv:2508.19419, 2025).

Ringrose, P., Atbi, M., Mason, D., Espinassous, M., Myhrer, Ø., Iding, M., Mathieson, A., Wright, I., 2009. Plume development around well KB-502 at the in Salah co2 storage site. First Break 27 (1).

Shafiei, A., Dusseault, B., Kosari, M.E., Taleghani, N.M., 2018. Natural fractures characterization and in situ stresses inference in a carbonate reservoir—an integrated approach. Energies 11 (2), 312.

Shi, J., Durucan, S., 2005. Co2 storage in deep unminable coal seams. Oil Gas Sci. Technol. 60 (3), 547–558.

Span, R., Wagner, W., 1996. A new equation of state for carbon dioxide covering the fluid region from the triple-point temperature to 1100 k at pressures up to 800 MPA. J. Phys. Chem. Ref. Data 25 (6), 1509–1596.

Vermeulen, T., 1953. Theory for irreversible and constant-pattern solid diffusion. Ind. Eng. Chem. 45 (8), 1664–1670.

Wadsley, W., 1980. Modelling reservoir geometry with non-rectangular coordinate grids. In: SPE Annual Technical Conference and Exhibition? SPE–9369. SPE.

Xu, Y., Fernandes, B.R.B., Marcondes, F., Sepehrnoori, K., 2019. Embedded discrete fracture modeling for compositional reservoir simulation using corner-point grids. J. Pet. Sci. Eng. 177, 41–52.

Xu, Y., Sepehrnoori, K., 2019. Development of an embedded discrete fracture model for field-scale reservoir simulation with complex corner-point grids. SPE Journal 24 (4), 1552–1575.

Zhang, Y., Yang, S., Luo, Y., Han, Y., Tian, L., Liu, Q., Gao, X., Shen, B., Yang, R., Li, J., 2025. Visual characterization, exergy and mechanism analysis of in-situ nonequilibrium dynamic phase-behavior of co2-oil. Energy 136560.

Zimmerman, R.W., Chen, G., Hadgu, T., Bodvarsson, G.S., 1993. A numerical dual-porosity model with semianalytical treatment of fracture/matrix flow. Water Resour. Res. 29 (7), 2127–2137.